

Galactic Outflow Emission Line Profiles: Evidence for Dusty, Radiatively-Driven Ionized Winds in Mrk 462

Sophia R. Flury¹,^{*} Edward C. Moran,² Miriam Eleazer^{1,2}

¹Department of Astronomy, University of Massachusetts Amherst, Amherst, MA 01002, United States

²Astronomy Department, Wesleyan University, Middletown, CT 06459, United States

Accepted XXX. Received YYY; in original form ZZZ

ABSTRACT

Over the past half century, gas outflows and winds have been observed as asymmetric emission lines in a wide range of astrophysical contexts, including galaxies and early-type stars. While P Cygni lines are modeled and understood with physically-motivated profiles under the Sobolev approximation, asymmetric nebular lines are not. Previous studies of galactic outflows using nebular emission lines have made physically unjustified assumptions about the shape of the line profile. These approaches limit assessment of outflow properties and do not connect observations to the underlying physics. The physical complexity of galactic outflows requires a more robust approach. In response to this need, we present a novel profile for modeling nebular emission lines which is generalized yet physically motivated and provides insight into the underlying mechanisms of galactic outflows. To demonstrate the usefulness of this profile, we fit it to the asymmetric nebular lines observed in the nuclear region of Mrk 462, a starburst-AGN composite galaxy. From analysis of the best-fit profile, we conclude that the observed profile arises from a dusty radiation-pressure-driven outflow with a terminal velocity of 750 km s^{-1} . This outflow, while weak by some standards, is still sufficiently strong to regulate star formation and black hole growth in the host galaxy by removing gas from the inner few kiloparsecs. Outflows like the one we observe and characterize in Mrk 462 are crucial to our understanding of episodic gas-fueled activity in galactic nuclei, which undoubtedly plays a pivotal role in galaxy evolution.

Key words: galaxies: evolution – galaxies: kinematics and dynamics – galaxies: nuclei – galaxies: active – galaxies: starburst – ISM: jets and outflows

1 INTRODUCTION

Gas outflows from galaxies are nearly ubiquitous and likely play a fundamental role in galaxy evolution from triggering bursts of star formation to temporary or even permanent quenching. So significant is the impact that the 2020 Decadal Survey identified the origins, nature, and effects of these outflows as one of the pressing open science questions in extragalactic astronomy. Understanding the underlying mechanisms and properties of outflows is important for establishing in detail the relationship between these energetic phenomena and their host galaxies.

One of the most insightful diagnostics of outflow properties has been UV absorption-line spectroscopy. Many studies have simplified their assessment of these features using non-parametric approaches (e.g., Steidel et al. 2010; Heckman et al. 2011, 2015; Henry et al. 2015; Chisholm et al. 2017b; Jaskot et al. 2017) or by fitting one or more Gaussian or Voigt components to the line (e.g., Rupke et al. 2002; Martin 2005; Rupke & Veilleux 2005; Chisholm et al. 2015; Gazagnes et al. 2018; Xu et al. 2022). With detailed, physical models of outflows in recent years, absorption and P-Cygni line analysis (predominantly in the UV, although optical Na I lines have been employed as well) has led to characterization of the mechanisms underlying the outflow (Vink et al. 2001; Steidel et al. 2010; Prochaska et al. 2011;

Scarlatà & Panagia 2015; Chisholm et al. 2016; Carr et al. 2018; Vink & Sander 2021). However, with the anticipated loss of *HST* (our sole UV observing facility) in the near future and accompanied by the advent of *JWST*, emission lines in other rest-frame regimes must be used for detailed investigations of outflows going forward.

Most previous studies of outflows using nebular emission lines have provided little physical justification for the particular line profiles adopted. Pelat & Alloin (1980) and Pelat et al. (1981) established the use of multiple Gaussian components for achieving a better description of the line profile (now commonplace in the galactic outflow literature, e.g., Villar-Martín et al. 2011; Amorín et al. 2012; Liu et al. 2013; Harrison et al. 2014; Gallagher et al. 2019; Eggen et al. 2022; Armus et al. 2022; Mainali et al. 2022). Others use the less physically-motivated Gauss-Hermite formalism from van der Marel & Franx (1993) to merely “account” for line asymmetries instead of inferring properties of the outflow (also prevalent in the literature, e.g., Salviander et al. 2007; Riffel 2010; Ludwig et al. 2012; Schönell et al. 2019; Ruschel-Dutra et al. 2021). Alternatively, emission-line profile flux quantiles and line widths can be used to characterize outflows (e.g., Heckman et al. 1981; Whittle 1985; Veilleux 1991; Liu et al. 2013; Harrison et al. 2014; Veilleux et al. 2020; Ruschel-Dutra et al. 2021). While this non-parametric approach avoids the need for assumptions about the profile, its pure empiricism cannot fully connect observations with the underlying physics of the presumed outflow that produces them.

*E-mail: sflury@umass.edu

Seeing the lack of clear physical motivation, [Krumholz et al. \(2017\)](#) developed model profiles for atomic and molecular nebular lines that relate directly to the physics of outflows. However, their profiles require assumptions about the driving mechanisms (winds vs radiation), physics (point mass vs isothermal potentials) and geometry (conserved angle vs conserved solid angle) a priori. Despite the successful application of the [Krumholz et al. \(2017\)](#) profiles to the outflows observed in starburst galaxy M82, this highly tailored approach lacks the flexibility and wide applicability offered by the other methods described above. Moreover, it cannot provide general insight regarding the origin of the observed outflow.

There is obvious need for a model that properly relates the physics of galactic outflows to observed nebular emission lines *without* making assumptions about the mechanisms beforehand. Further exacerbating the problem is the need for such a model to contain few parameters and to be flexible, i.e., to readily fit data without substantial tweaking. To address these needs, we have developed a novel model emission-line profile for use in analyzing ionized outflows. In §2, we outline the formalism for a nebular emission-line profile derived from solutions to the equation of motion for interstellar winds. Then, in §3, we demonstrate the application of this model to medium resolution rest-frame optical spectra of the nearby dwarf galaxy Mrk 462, which displays asymmetric emission-line profiles indicative of outflows (Eleazer et al. in prep). Interestingly, Mrk 462 possesses both an AGN and nuclear star formation ([Moran et al. 2014](#), Eleazer et al. in prep); it thus provides a unique context for the investigation of outflows in which the outflow origins and mechanisms are ambiguous (Eleazer et al. in prep). Finally, we assess the underlying physics implied by fits to the data in §4. From the best-fit velocity profile, we find that dusty radiation pressure is the most likely driver of the observed outflow, favoring a clumpy cloud geometry over a homogeneous one. We conclude that, while weak in relative terms, the outflow in Mrk 462 is sufficiently strong to expel gas from the galactic gravitational potential, thereby influencing star formation and/or AGN activity.

2 A NEBULAR LINE PROFILE FOR GALACTIC OUTFLOWS

Many previous studies of photoionized outflows with nebular emission lines have demonstrated asymmetry in the line profile, notably in [O III] λ 5007, where the blue wing is more prominent than the red (e.g., [Veilleux 1991](#); [Villar-Martín et al. 2011](#); [Liu et al. 2013](#); [Harrison et al. 2014](#); [Gallagher et al. 2019](#); [Leung et al. 2019](#); [Armus et al. 2022](#), although see [Ruschel-Dutra et al. 2021](#) for red-winged profiles). This asymmetric blue wing is ubiquitously attributed to outflows since neither rotation nor mergers can account for the observed profile (e.g., [Heckman et al. 1981](#); [Liu et al. 2013](#); [Rupke & Veilleux 2013](#); [Harrison et al. 2014](#)). These observed asymmetric emission lines require a new, physically motivated line profile to obtain insight into the properties and driving mechanism(s) of the underlying outflow. As discussed in §1, such a line profile must satisfy two requirements. First, it must not presume the underlying physics. Second, it must be flexible by having clear formalism and few parameters to ensure versatility in the analysis of line profiles in a wide variety of systems.

Models for outflow profiles have been previously presented in the literature. However, these rely on assumptions about the underlying physics and geometry of the outflow, critically, the mechanism driving the outflow and whether energy or momentum is conserved in the process. Different mechanisms invoked in line profiles include

layered turbulence ([Binette et al. 2009](#)), radiation pressure and hot winds ([Krumholz et al. 2017](#)). Our aim, motivated by the composite activity in Mrk 462, is to model outflows without making assumptions about how the observed line profiles are produced. In objects like Mrk 462, the relationship between the observed line profile and the origins of the outflow becomes increasingly unclear: stellar feedback, AGN feedback, supernovae, or some combination of all three, could provide the initial acceleration. As a result, we require a physically-motivated line profile model which is wholly agnostic to the underlying mechanisms.

Below, we describe a velocity profile which is both a solution to the equation of motion for a galactic outflow and independent of the underlying physics. We also define a density profile to express the distribution of particles within the outflow. Then, we illustrate how to compute a nebular emission line profile from the velocity and density profiles. Finally, we elaborate on numerical methods to solve the relevant equations rapidly and accurately for the purpose of fitting our model to the observed emission lines.

2.1 Velocity and Density Profiles

Velocity profiles for winds can take on a variety of shapes arising from different treatments of the wind equations of motion (e.g., [Castor et al. 1975](#); [Lamers & Morton 1976](#); [Abbott 1977](#); [Barlow & Cohen 1977](#)). The simple β form of the velocity profile arises from a generalization of these solutions without loss of physical insight ([Castor & Lamers 1979](#); [Pauldrach et al. 1986](#)) and has become ubiquitous in the study of stellar winds and galactic outflows (e.g., [Vink et al. 2001](#); [Vink & Sander 2021](#); [Chisholm et al. 2016, 2017b, 2018a](#), see similar formalism in [Steidel et al. 2010](#); [Prochaska et al. 2011](#)). It is thus justifiable to adopt

$$v(r) = v_{\infty} \left(1 - \frac{R_0}{r} \right)^{\beta} \quad (1)$$

where R_0 is the radial distance from the progenitor at which the outflow begins (the “launch” radius) and v_{∞} is the asymptotic terminal velocity reached in the limit of $r \rightarrow \infty$. Typical values for β range from 0.5 ([Castor et al. 1975](#); [Abbott 1977](#); [Chisholm et al. 2016](#)) to 4 ([Barlow & Cohen 1977](#)) with 1 often chosen for theoretical models of line profiles produced by winds ([Castor & Lamers 1979](#); [Lamers et al. 1987](#); [Vink et al. 2001](#)) as values of 0.8-1 are consistent with observed stellar P Cygni profiles ([Pauldrach et al. 1986](#)). Under the Sobolev approximation ([Sobolev 1960](#), although [Sobolev 1944, 1957](#) provide earlier renditions), the outflow velocity is solely responsible for producing the observed line profile because the velocity gradient is much steeper than any local velocities (e.g., thermal or turbulent Doppler broadening). Thus, the above velocity law can be taken as characteristic of the observed line profile (cf. [Noerdlinger & Rybicki 1974](#); [Mihalas et al. 1975](#); [Lamers et al. 1987](#); [Prochaska et al. 2011](#); [Scarlata & Panagia 2015](#), for the same assumption).

For simplicity, gas number density is also assumed to follow a power law such that

$$n(r) = n_0 \left(\frac{R_0}{r} \right)^{\alpha}, \quad (2)$$

where n_0 is the gas number density at R_0 , again a common choice in the literature (e.g., [Scarlata & Panagia 2015](#); [Chisholm et al. 2016](#)). Simple algebra gives the density in the wind as a function of velocity such that

$$n(v) = n_0 \left[1 - \left(\frac{v}{v_{\infty}} \right)^{1/\beta} \right]^{\alpha} \quad (3)$$

(see Equation 11 in Chisholm et al. 2016, for a comparable result). As expressed here, typical values for α range from 1 to 9 with 2 being characteristic of a mass-conserving, isothermal sphere (see, e.g., Rupke et al. 2005b; Prochaska et al. 2011; Chisholm et al. 2016; Krumholz et al. 2017) and larger values indicating mass removal by mechanisms such as fountains (e.g., Leroy et al. 2015; Chisholm et al. 2016).

In some cases, continuity has been invoked to relate α and β , thereby reducing the number of free parameters (e.g., Scarlata & Panagia 2015; Carr et al. 2018). While it would be lucrative to reduce the dimensionality¹, the combined profiles in Equations 1–2 prohibit doing so: the extremes of $r = R_0$ and $r \rightarrow \infty$ yield momentum densities $n\nu$ of zero while interior to these extremes, the momentum density is non-zero, a clear violation of continuity. As an alternative to continuity, we could simply assume some value for α . However, leaving α free adds just one parameter more than either adding an additional Gaussian component or employing the Gauss-Hermite formalism. Moreover, leaving α free allows us to avoid any additional assumptions about the underlying physics of the outflow. We demonstrate below that α correlates with v_∞ rather strongly (see §3, Figure 2). Any presumed value or relationship for α thus biases the terminal outflow velocity obtained from the model. Therefore, we choose to include α as a distinct, free parameter in our model.

2.2 Radiative Transfer

Gas at any given velocity will produce line emission by the same mechanism. The nebulae surrounding star-forming regions or AGN are optically thin to non-resonant line emission, so no scattering or escape effects need to be included when calculating the emergent flux density². Adapting Equation 5.41 in Osterbrock & Ferland (2006, see also Equation 3 in Peimbert et al. 2017), the total flux density at any wavelength λ is given by the integral over all line-emitting clouds with a velocity v , projected velocity $u = (\lambda - \lambda_0)c/\lambda_0$, and emission coefficient j_λ such that

$$F_\lambda = 4\pi \int_{\nu} j_\lambda(v) dv \quad (4)$$

for an optically thin emission line. Following the formalism for nebular emission lines in Osterbrock & Ferland (2006), j_λ for nebular lines like H α or [O III] is given by

$$j_\lambda = \varepsilon n_e n_\chi \quad (5)$$

for a radiative electronic transition of energy $h\nu$, emissivity ε related to the recombination rate or the collisional excitation rate (see Equations 4.14 and 3.29, respectively, in Osterbrock & Ferland 2006, cf. Equation 3 in Peimbert et al. 2017), electron density n_e and density of ion χ . Under the Sobolev approximation, local variations in n_e relative to n_χ within a single cloud are negligible. Therefore, we assume that n_e and n_χ are equivalent and can therefore be expressed by the density term $n(r) \propto n_e \propto n_\chi$. This assumption allows us to rewrite the emergent flux density as

$$F_\lambda = F \phi_\lambda(\lambda_0, \alpha, \beta, v_\infty) \quad (6)$$

¹ Invoking continuity or any other physical assumption is not lucrative in the least for our purposes: we want to assume as little as possible a priori about the underlying physics.

² Resonant lines, which are not optically thin, do require such treatment, typically under limiting assumptions to obtain an additional factor of $(1 - \exp(-\tau))\tau^{-1}$ in the velocity integral (e.g., Scarlata & Panagia 2015; Carr et al. 2018).

where ϕ_λ is the line profile at any given λ due to a combination of velocities and densities projected onto the line of sight, and $F = 4\pi h\nu \varepsilon n_e n_\chi$ is the integrated flux of the outflow line emission.

To obtain the line profile, we consider a spherical geometry with density defined in terms of the radial distance from the outflow source. Doing so allows us to integrate the squared density profile over the range of all velocities $v/v_\infty = w$ that are projected to the observed velocity u . The maximum value of w at any given u in the line profile is necessarily unity since the outflow, by definition, cannot exceed its own terminal velocity. Because minimum value of w is not a constant, we simply denote it as w_ℓ . The resulting expression for ϕ is then

$$\phi_\lambda = K^{-1} \int_{w_\ell}^1 [1 - w^{1/\beta}]^{2\alpha} dw \quad (7)$$

where K is a normalization constant ensuring $\int_\lambda \phi_\lambda d\lambda = 1$.

For the blueshifted emission (i.e., outflow moving toward the observer), the minimum velocity w_ℓ is simply the absolute value of the observed velocity, giving

$$w_\ell = |u|. \quad (8)$$

For the redshifted emission (i.e., outflow receding away from the observer), occultation of the outflow by the outflow source (e.g., an AGN or young stellar population embedded in optically thick material) increases w_ℓ by a cosine projection of the source radius at the observed velocity u (cf. Scarlata & Panagia 2015; Carr et al. 2018, for similar treatment with resonant lines). The resulting expression for w_ℓ is

$$|u| = \frac{w_\ell}{x(w_\ell)} \sqrt{x(w_\ell)^2 - 1} \quad (9)$$

where

$$x = \frac{r}{R_0} = (1 - w^{1/\beta})^{-1} \quad (10)$$

is the dimensionless radius.

Finally, the line profile normalization constant K is given by integrating ϕ_λ over all possible λ which satisfy $u \in [-1, 1]$, i.e., $\lambda \in [\lambda_{-\infty}, \lambda_{+\infty}]$ where $\lambda_{\pm\infty} = \lambda_0(1 \pm v_\infty/c)$. Furthermore, the integral of ϕ_λ over λ must be broken down into blueshifted ($\lambda \in [\lambda_{-\infty}, \lambda_0]$) and redshifted ($\lambda \in [\lambda_0, \lambda_{+\infty}]$) components to account for the difference in velocity limits (recall that this difference arises from occultation of the outflow by the outflow source).

As a reference to the reader, we illustrate effects of the density and velocity profile slopes on the emergent profile for the [O III] λ 5007 emission line in Figure 1. Decreasing either the velocity profile slope β or the density profile slope α increases the prominence of the profile wings at fixed v_∞ .

2.3 Implementation

To obtain w_ℓ for the redshifted profile component ($\lambda \in [\lambda_0, \lambda_{+\infty}]$), we use Brent's method with brackets of $w_\ell \in [u, 1)$ to determine the value of w_ℓ which best satisfies Equation 9. Typically, Brent's method converges on a solution for w_ℓ within $\lesssim 10$ iterations for any given u .

To solve the integral term in Equation 7 for given λ_0 , α , β , and v_∞ , we use the Romberg integration method of adaptive step sizes for definite integrals. This approach optimizes the values of w where the integrand is evaluated over $w \in [w_\ell, 1]$ while minimizing the number of calculations necessary to converge on the solution. For ϕ_λ , this

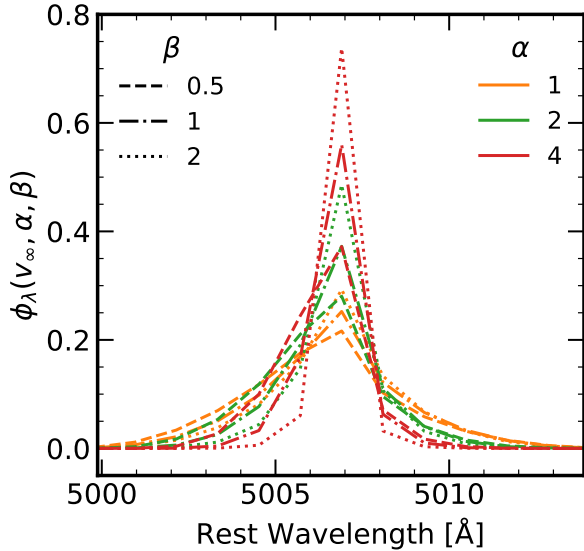


Figure 1. Effects of varying density profile slope α and velocity profile slope β on the [O III] emission line profile emergent from the outflow. Example profiles assume a spectral resolution of $R = 1688$ to emulate an observation with the *Gemini*/GMOS B600+G5307 grating.

method converges within $N \lesssim 8$ iterations with the total calculations of the integrand equal to $\sum_{i=0}^{N-1} 2^i + 1$.

For the normalization coefficient K , we use a simple trapezoid integral of the ϕ_λ computed above. The trapezoid method is preferred over more sophisticated methods due to the cusp at $\lambda = \lambda_0$. The simplicity of the trapezoid method also requires very few calculations without significant loss of accuracy.

To facilitate reproducible results, we include in Appendix A an example implementation of the emergent line profile formalism in python based on the numerical methods outline here.

3 APPLICATION TO MRK 462

Mrk 462 is a line-emitting dwarf galaxy with $M_\star = 5.5 \times 10^9 M_\odot$ at a distance of 41.3 Mpc. Both AGN and star-formation activity are evident in the rest-frame optical SDSS spectrum, with AGN signatures indicating the presence an intermediate mass black hole (Moran et al. 2014). Eleazer et al (in prep) observed Mrk 462 for 1.4 hr on 2012/04/03 using *Gemini*/GMOS with the B600+G5307 grating ($R = 1688$ covering 4200–7100 Å) to obtain integral field unit spectra covering the central kiloparsec of Mrk 462 in a $5'' \times 3.5''$ (1 kpc \times 0.6 kpc at a distance of 41.3 Mpc) field of view. To maximize S/N, we proceed using the co-addition of all the *Gemini*/GMOS IFU spaxels. For details of the data reduction and results, we refer the reader to their paper. During their efforts to determine the emission line fluxes, they discovered an asymmetric nebular emission line profile present in the strong forbidden narrow lines. The persistence of the asymmetric profile across the central kiloparsec of Mrk 462 indicates a large-scale outflow akin to those observed in AGN and starburst galaxies (e.g., Heckman et al. 1981, 1990; Rupke & Veilleux 2011, 2013). Mrk 462 thus presents a unique opportunity to demonstrate the use of our model to derive outflow properties from nebular emission line profiles.

To begin our analysis, we fit each line in the [O III] $\lambda\lambda 4959, 5007$

Table 1. Quantiles of the posterior of parameters for the combined Gaussian and outflow profiles for the [O III] profile observed in Mrk 462.

	quantile		
	0.16	0.5	0.84
σ_v [km s $^{-1}$]	67.604	67.758	67.911
v_∞ [km s $^{-1}$]	733.629	745.635	757.960
α	1.093	1.122	1.151
β	1.338	1.369	1.400
f	0.495	0.498	0.501

doublet with a coaddition of the outflow $\phi_{\lambda o.f.}$ defined in Equation 7 and a Gaussian core $\phi_{\lambda \text{Gauss}}$ to account for random motions of nebular gas not contained in the outflow, i.e.,

$$F_\lambda = F_0 [f\phi_{\lambda \text{Gauss}} + (1 - f)\phi_{\lambda o.f.}] + C_\lambda \quad (11)$$

where f is the fraction of total flux F_0 contained in the Gaussian component of the line and C_λ is the continuum flux. Fitting the [O III] doublet lines provides three advantages: (i) both are well-detected; (ii) both are emitted by the same ion species with identical excitation mechanisms, meaning the physical parameters for $\phi_{\lambda \text{Gauss}}$ and $\phi_{\lambda o.f.}$ are the same; and (iii) the F_0 and λ_0 of each line are related to those of the other by well-known atomic physics. Therefore, including both lines doubles the amount of data used the fit without adding additional variables or substantial uncertainty, thereby providing more robust constraints on the parameters.

We sample the posterior on parameters λ_0 , σ_v , v_∞ , α , β , f , and C_λ using the python MCMC package `EMCEE` (Foreman-Mackey et al. 2013). For robustness, we use 32 walkers, assume a burn-in of 10^3 steps, and a take a subsequent 10^4 steps. We assume a uniform prior with the requirements that fluxes be positive, α and β remain in the possible range of values (0 to 9 and 0 to 4, respectively, following the literature evaluations discussed in §2.1, cf. Chisholm et al. 2016), and the Gaussian velocity width σ_v not exceed v_∞ . Results of this sampling are listed in Table 1 with a posterior map shown in Figure 2. We show the corresponding best-fit profile in Figure 3.

The constraints on each of the parameters are quite good, with uncertainties of only a few percent. Moreover, the posterior samples appear quite normal and, by extension, multivariate normal. While most parameters exhibit a mild covariance, the α and v_∞ posteriors are strongly positively correlated. Physically, this correlation may indicate that the density profile affects the terminal velocity of the outflow. The implication of such a relationship is that the acceleration of clouds in the outflow persists well beyond the initial launch radius.

As evident in Figure 3, the profile reproduces the asymmetric wings of the [O III] doublet with great accuracy. The best-fit profile recovers the observed doublet flux with a median residual of 2.47%. Median uncertainties in the flux are 1.37%, meaning that, characteristically, the profile flux is within 2σ of that observed. Such excellent agreement demonstrates that our flexible outflow profile model successfully describes the observed profile without making assumptions about the underlying mechanisms.

4 INTERPRETING THE OUTFLOW PROFILE

Having successfully fitted the Mrk 462 [O III] doublet with our outflow-motivated line profile, we now have the opportunity to evaluate the physical nature of the outflow.

First and foremost, we need to demonstrate how the best-fit parameters translate into properties of the outflow, namely the mass outflow rate and momentum and energy injection rates. Moreover,

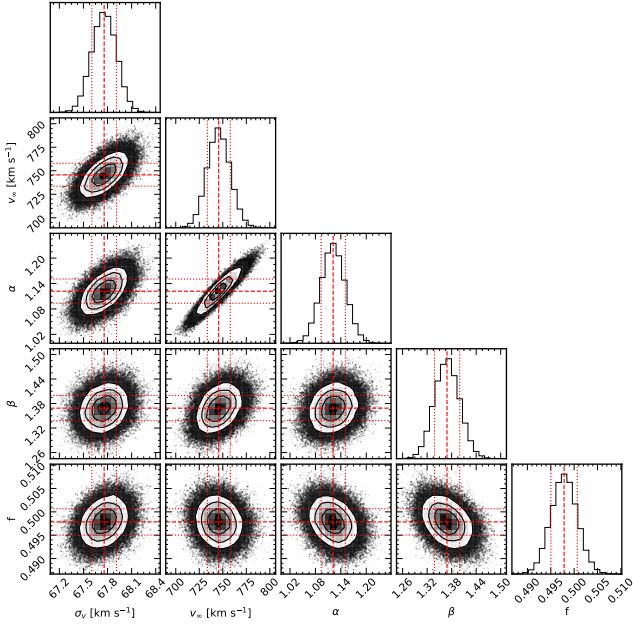


Figure 2. Posterior of the dynamically-relevant profile parameters for the [O III] $\lambda\lambda 4959, 5007$ doublet. Velocities in units of km s^{-1} . Best-fit values are indicated by red dashed lines while 0.1587 and 0.8413 quantiles are shown as red dotted lines. Values relevant to the dynamics of the ionized gas are listed Table 1.

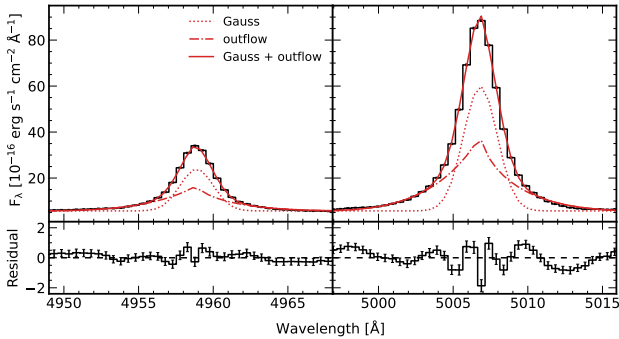


Figure 3. *Top:* Best-fit line profiles (red) overlaid on the [O III] doublet flux measured in the nucleus of Mrk 462 (black). Outflow component is the dash-dotted line. Gaussian component is the dotted line. Total is the solid line. *Bottom:* Residual flux obtained by taking the difference between the total fit profile and the observed flux. Error bars in all panels indicate the 3σ uncertainty in flux density in each pixel.

we are concerned with how the derived properties for Mrk 462 compare to properties of outflows observed in other galaxies. Placing Mrk 462 into a more general context of galactic outflows in this manner is critical for two reasons: (i) demonstrating that our novel analysis of the [O III] emission line profile is capable of providing insight into outflow properties and (ii) determining whether the outflow Mrk 462 scales appropriately with those observed in other galaxies. For these purposes, we draw on results in the literature for large samples of galactic outflows as measured via Na I D (Rupke et al. 2005a; Heckman et al. 2015) and UV absorption lines (Chisholm et al. 2017a; Xu et al. 2022).

Because these measurements span various ISM phases, comparing them to our own results bears justification. Rupke et al. (2005a) demonstrate in their Figure 17 that the Na I D absorption line profiles are consistent with the blue-shifted wings of [N II] and [O III] emission lines in the same galaxies, indicating that both the neutral and ionized species trace galactic winds with similar outflow velocities. Similarly, Heckman et al. (2015) find comparable profile shapes among various UV absorption lines arising from ions having a wide range of ionization potentials (8.151 to 33.492 eV). Previous studies have compared outflows measured by Na I D and UV absorption lines from ion species of different ionization potentials (e.g., Xu et al. 2022), finding relatively consistent agreement between galaxy properties like stellar mass and star formation rate and outflow properties like velocity and momentum injection rate. Therefore, we can confidently compare results from measurements of various outflow phases to those from the ionized outflow traced by [O III] in Mrk 462.

Secondly, we need to connect the best-fit velocity and density profiles to the underlying astrophysical processes. Specifically, what drives the outflow, and what are its effects on its host galaxy? To answer these questions, we draw on physically-based velocity profiles derived by Murray et al. (2005) from the equation of motion for a variety of driving mechanisms in order to assess the implications of the observed line profile.

4.1 Outflow Momentum and Energy

To determine the outflow momentum and energy, we follow the formalism outlined in Rupke et al. (2002, 2005b). First, we determine the mass outflow rate from the column density (found by integrating the density profile from R_0 to r) and outflow velocity such that

$$\dot{M} = \Omega R_0 \mu m_{\text{H}} N_{\text{H}} v_{\text{out}} = 4\pi R_0^2 \mu m_{\text{H}} n_0 v_{\infty} \mathcal{R}(x; \alpha, \beta) \quad (12)$$

for solid angle $\Omega = 4\pi$ sr (cf. Equations 1-3 in Rupke et al. 2005b). The function \mathcal{R} expresses the radial dependence of \dot{M} where

$$\mathcal{R}(x; \alpha, \beta) = \begin{cases} \ln(x) \left(1 - \frac{1}{x}\right)^{\beta} & \alpha = 1 \\ \frac{1}{1-\alpha} \left[\left(\frac{1}{x}\right)^{\alpha-1} - 1 \right] \left(1 - \frac{1}{x}\right)^{\beta} & \alpha \neq 1 \end{cases} \quad (13)$$

from the velocity profile (Equation 1) and the integral of the density profile (Equation 2) with respect to $x = r/R_0$. Two key differences distinguish our expression for \dot{M} from that given by Rupke et al. (2002, 2005b): (i) we do not assume an isothermal potential ($\alpha = 2$) and (ii) we do not assume a radially constant velocity profile.

Previous studies of outflows have either assumed some value of R_0 (often 1-5 kpc, e.g., Rupke et al. 2005a) or used the UV half-light radius (i.e., the “starburst” radius) to determine R_0 under the premise that this value is similar to the launch radius regardless of mechanism (e.g., Heckman et al. 2015; Xu et al. 2022). For R_0 , we consider the SDSS u band Petrosian radius of $2.7''$, which corresponds to ~ 0.54 kpc for Mrk 462. This value is consistent with UV half-light radii measured for other galactic outflows (Heckman et al. 2015; Xu et al. 2022), which suggests our assumed R_0 is appropriate. However, Heckman et al. (2015) argue that R_0 must be scaled in order to properly derive outflow properties. At what radius do we evaluate \dot{M} ? Both $x = 1$ (i.e., $r = R_0$) and $x \rightarrow \infty$ will yield meaningless mass outflow rates (see discussion in §2.1). We therefore choose the value x_{out} which maximizes the momentum density nv . For the best-fit values of α and β , we list results for x_{out} and the corresponding outflow velocity v_{out} in Table 2. Interestingly, our value for x_{out} is close to the factor of 2 assumed in previous studies (e.g., Heckman et al. 2015; Xu et al. 2022); however, given the dependence of x_{out}

Table 2. Outflow properties derived from best-fit outflow profile for $n_0 = 41 \text{ cm}^{-3}$ and $R_0 = 0.539 \text{ kpc}$ from the u -band Petrosian radius. Quantiles determined by propagating the MCMC samples of the posterior on the outflow profile parameters.

	quantile		
	0.16	0.5	0.84
x_{out}	2.183	2.220	2.258
$v_{out} [\text{km s}^{-1}]$	326.888	328.619	330.385
$\mathcal{R}(x_{out}; \alpha, \beta)$	0.321	0.335	0.350
$\log \dot{M} [\text{M}_\odot \text{ yr}^{-1}]$	2.739	2.752	2.766
$\log \dot{p} [\text{dyne}]$	36.055	36.068	36.083
$\log \dot{E} [\text{erg s}^{-1}]$	43.322	43.337	43.352

and the related momentum distribution on α and β , we caution against simply assuming a factor of 2. In Appendix B, we elaborate on the effects of α and β on x_{out} .

We obtain the particle density n_0 from an emission measure argument. Following Equation 5, the emission measure $n_e n_p$ can be obtained using the emission coefficient and luminosity for $[\text{O III}]\lambda 5007$ such that

$$n_0^2 \approx n_e n_p = \frac{L_{\lambda 5007}(1-f)}{4\pi\epsilon R_0^2 \Delta R \epsilon_{\lambda 5007}} \frac{\text{H}^+}{\text{O}^{++}} \quad (14)$$

where the ionic abundance O^{++}/H^+ scales $n_{\text{O}^{++}}$ to $n_p \approx n_e$, $\Delta R \sim 1 \text{ pc}$ is the characteristic cloud size (see, e.g., Klein et al. 1994; Nakamura et al. 2006), and $\epsilon \sim 0.01$ is the fraction of the outflow volume populated by clouds (i.e., the filling factor, e.g. Osterbrock 1991)³. The ionic abundance O^{++}/H^+ can be obtained using the flux and emissivity ratios for $[\text{O III}]$ and $\text{H}\beta$ such that

$$\frac{\text{O}^{++}}{\text{H}^+} = \frac{F_{\lambda 5007}}{F_{\text{H}\beta}} \frac{\epsilon_{\text{H}\beta}}{\epsilon_{\lambda 5007}} \quad (15)$$

for some assumed electron temperature (Equation 5.41 Osterbrock & Ferland 2006, see also Equation 16 in Peimbert et al. 2017). Using the flux ratio $F_{[\text{O III}]\lambda 5007}/F_{\text{H}\beta} = 2.92$ reported in Moran et al. (2014) and ϵ calculated using PYNEB (Luridiana et al. 2015) assuming $1.5 \times 10^4 \text{ K}$ for the electron temperature (based on our estimate that the $[\text{O III}]\lambda 4363$ auroral line flux is $\approx 2\%$ that of the $\lambda 4959, 5007$ doublet, which is consistent with analysis of the SDSS spectrum included in Moran et al. 2014), we obtain $\text{O}^{++}/\text{H}^+ = 3 \times 10^{-5}$. Finally, we obtain a density of $n_0 \approx 41 \text{ cm}^{-3}$, which is similar to the densities of 20 to 30 cm^{-3} in outflows Chisholm et al. (2018b) studied using photoionization models.

With density and radius in hand, we can calculate the mass outflow rate \dot{M} . We find $\dot{M} = 179 \text{ M}_\odot \text{ yr}^{-1}$ for Mrk 462. The momentum and energy injection rates are given by Equations 9 and 11, respectively, in Rupke et al. (2005b) where the former is

$$\dot{p} = \dot{M} v_{out} \quad (16)$$

and the latter is

$$\dot{E} = \dot{M} \left[\frac{1}{2} v_{out}^2 + \frac{3}{2} \sigma_v^2 \right]. \quad (17)$$

We assume (somewhat naively) that the turbulent energy within the outflow is equivalent to the velocity dispersion of the Gaussian component fit to the profile in the previous section. Results for \dot{p} and \dot{E} are listed in Table 2.

³ To calculate n_0 from the expected value of the density, one scales n_0 by a factor of $(\alpha + 2)^{1-1/\alpha}$. For the value of α observed in the Mrk 462 $[\text{O III}]$ doublet, this factor is roughly unity.

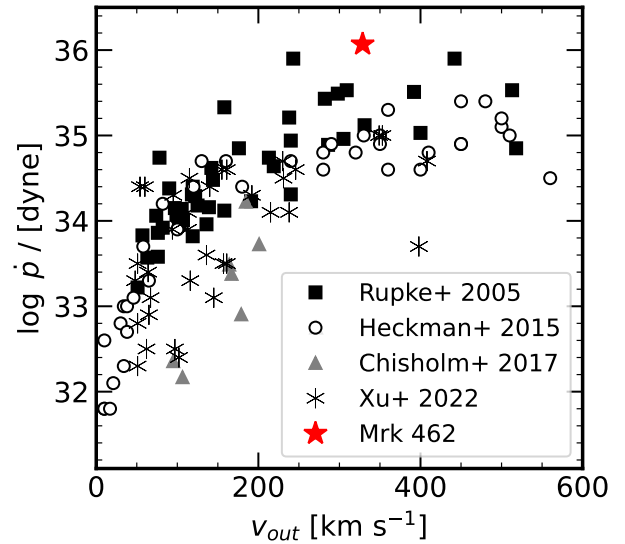


Figure 4. Momentum flux and velocity of the outflow in Mrk 462 (red star) compared to outflows observed in star-forming galaxies via absorption lines (squares Rupke et al. 2005b, open circles Heckman et al. 2015, triangles Chisholm et al. 2017a, asterisks Xu et al. 2022). Uncertainties obtained by propagating the MCMC samples of the best-fit parameters are smaller than the symbol for Mrk 462.

We compare the outflow properties in Table 2 to outflow properties in other galaxies in Figure 4. As evident in Figure 4, we find that the outflow in Mrk 462 has a momentum flux comparable to those of outflows observed in starburst galaxies via absorption lines. This result is compelling for two reasons. First, it validates our approach to deriving outflow properties from the observed line profile. Second, it places Mrk 462 into a rich context of starbursts, ULIRGs, and other star-forming galaxies. While we have not yet addressed what drives the outflow in Mrk 462, the outflow appears to be similar to those found in other galaxies.

The momentum fluxes and velocities of galaxy outflows form a sequence in Figure 4, with momentum flux increasing with increasing outflow velocity. The outflow in Mrk 462 occupies the high-velocity end of this sequence where the momentum flux changes much more gradually with velocity than it does below $\sim 200 \text{ km s}^{-1}$. To determine if outflows with momentum fluxes and velocities similar to those of Mrk 462 can be characterized by similar density and velocity profiles, we predict sequences of \dot{p} from Equations 12-16 over a range of v_∞ for different values of α and β assuming a density of $n_0 = 10 \text{ cm}^{-3}$. We compare these predicted sequences of outflow properties to the observed distribution in Figure 5. As α decreases and/or β increases, the momentum flux and outflow velocity increase. This result suggests that the scatter in outflow \dot{p} is real and arises from distinct astrophysical scenarios such as wind-driven fountains or radiation-driven shells. While density may also account for the observed scatter, the density and velocity profiles combined in Equations 12-16 readily describe the shape of the distribution of \dot{p} over v_{out} . Thus, the sequence of outflow properties demonstrates a relationship between the underlying physics and the velocity and density profiles of the outflow.

To understand these outflow properties in the context of the host galaxy, one conventionally expresses the outflow velocity and momentum injection rate relative to dynamical values (see, e.g., Heck-

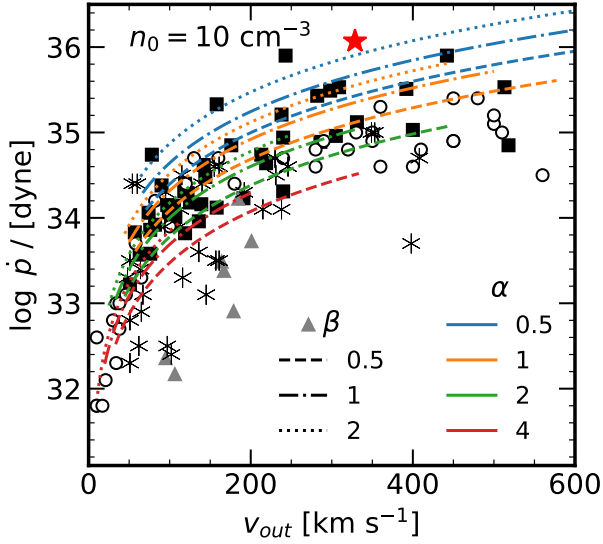


Figure 5. Effects of varying density profile slope α and velocity profile slope β on the observed momentum flux and outflow velocity for values of v_∞ ranging from 100 to 1,000 km s^{-1} . Symbols as in Figure 4.

man et al. 2015; Xu et al. 2022). For the velocity, the fiducial dynamical value is the circular velocity v_0 . We obtain the circular velocity for Mrk 462 using the stellar mass of $M_\star = 5.5 \times 10^9 M_\odot$ reported by Moran et al. (2014) and the empirical Tully-Fischer relation given by Equation 27 in Reyes et al. (2011) such that

$$\log v_0 = 2.141 + 0.278 [\log(M_\star) - 10.102] \quad (18)$$

with an accuracy of 0.096 dex⁴. Following Heckman et al. (2015), the critical injection rate of momentum to exceed the pull of gravity is given by

$$\dot{p}_0 = 4\pi R_0^2 \mu m_{\text{H}} n_0 v_0^2 \quad (19)$$

at the launch radius of the outflow. Combining the above expression with Equations 12 and 16, we obtain a relative momentum injection rate of

$$\frac{\dot{p}}{\dot{p}_0} = \mathcal{R}(x; \alpha, \beta) \left(\frac{v_\infty}{v_0} \right)^2 \left(1 - \frac{1}{x} \right)^\beta, \quad (20)$$

which we evaluate at $x = x_{\text{out}}$. We show predicted values of \dot{p}/\dot{p}_0 over a range of v_∞/v_0 in Figure 6. Strong outflows require $\alpha \leq 1$ and/or $\beta \geq 1$ with $v_{\text{out}}/v_0 \gtrsim 4$. Mechanisms associated with low α and high β may be more likely to drive strong outflows. This coupling between mechanism and outflow strength could even indicate that fountains, which are characterized by high α , might not be able to produce outflows capable of affecting the host galaxy.

From Figure 6, we arrive at several key realizations. Mrk 462 exhibits a relatively weak outflow, falling short of the Heckman et al. (2015) requirement that the momentum injection rate exceed the critical value due to gravity by more than an order of magnitude. Furthermore, Mrk 462 is *typical* in its outflow properties: many other

⁴ Note that this relation is specific to the photometric mass-to-light ratios used in Moran et al. (2014) to obtain the stellar mass of Mrk 462. That being said, results from this relation are within a few km s^{-1} to the approach used in Heckman et al. (2015); Xu et al. (2022), well within the ~ 0.1 dex uncertainty in both relations.

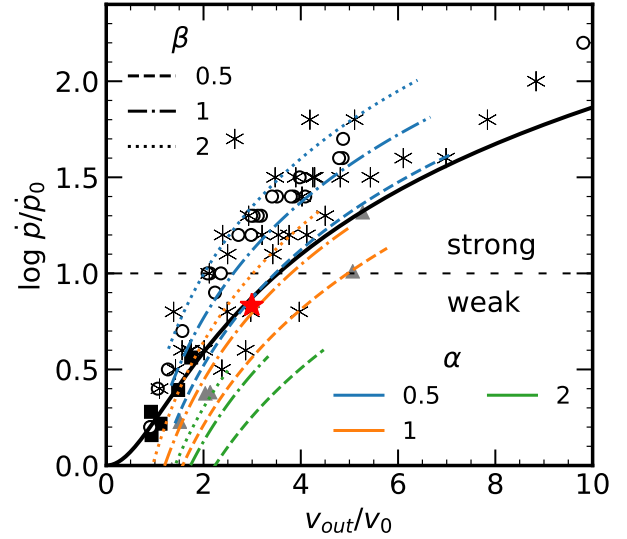


Figure 6. Momentum injection rate normalized to the critical momentum injection rate necessary to exceed the gravitational potential vs outflow velocity normalized to the rotational velocity of the galaxy inferred from the stellar mass. Thin dashed horizontal line is the demarcation between weak and strong outflows from Heckman et al. (2015). Solid line is the prediction for momentum-driven winds from Heckman et al. (2015). Predictions for various α and β values correspond to $v_\infty/v_0 \in [2, 10]$. Symbols as in Figure 4 but including only galaxies with $\dot{p} > \dot{p}_0$.

galaxies have comparable outflow strengths and relative velocities. Moreover, comparison with the Heckman et al. (2015) prediction for the wind equation of motion suggests that the momentum injection rate in Mrk 462 can be explained *solely* by a momentum-driven outflow. We address the mechanism which provides this momentum below in §4.2.

What remains to be learned from the outflow properties is the origin of the outflow. Mrk 462 exhibits both star-formation and AGN activity in its emission line spectrum, with young stars concentrated in a circumnuclear disk (Eleazer et al. in prep), meaning that nuclear star clusters and/or an accretion disk provide the momentum needed to produce the outflow. After correcting for extinction using the Reddy et al. (2016) law and the reddening inferred from the Balmer decrement, the GALEX (Martin et al. 2003) FUV flux suggests a star formation rate (SFR) of $0.25 M_\odot \text{ yr}^{-1}$ using the Calzetti (2013) conversion for a 1-10 Myr burst. This SFR assumes that all of the FUV flux is produced by young stellar populations, i.e., with no AGN contribution. Even in this maximal case, the measured SFR is much lower than one would expect given published trends between SFR and mass outflow rate, outflow velocity, and momentum injection rates (e.g., Heckman et al. 2015; Xu et al. 2022).

As discussed in §1, [O III] line profiles like that of Mrk 462 are found in many “pure” Seyferts. To determine if the outflow in Mrk 462 is consistent with AGN driving, we compare its energetics with those of [O III]-traced AGN outflows from Harrison et al. (2014) in Figure 7, inferring the bolometric AGN luminosity $L_{\text{AGN}} = 3.768 \times 10^{43} \text{ erg s}^{-1}$ for Mrk 462 from the flux of the narrow component of the [O III] line assuming the Heckman et al. (2004) bolometric correction. Given that the Harrison et al. (2014) method 2 is more comparable to our approach (i.e., it does not depend on the gas mass), this comparison suggests Mrk 462 is undergoing typical AGN-driven

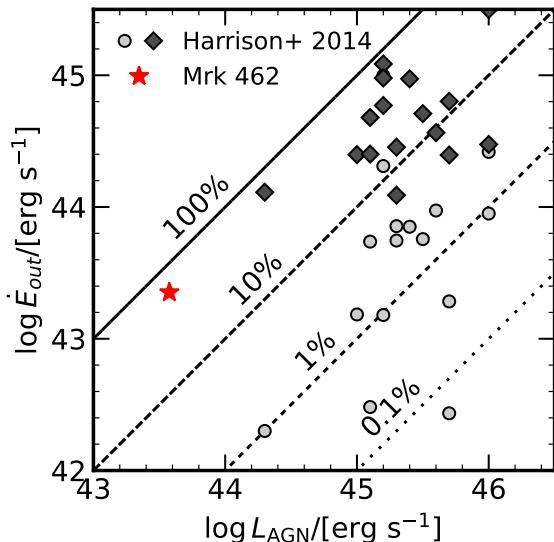


Figure 7. Comparison of outflow mechanical energy \dot{E} and bolometric AGN luminosity L_{AGN} for Mrk 462 (red star) and a sample of [O III]-traced AGN outflows from Harrison et al. (2014) with \dot{E} calculated using their methods 1 (light grey circles) and 2 (dark grey diamonds). We note that their method 2 is more comparable to ours than their method 1. Lines indicate constant values of outflow coupling efficiency.

feedback close to 100% outflow coupling efficiency (i.e., the AGN luminosity is closely linked to the outflow properties). We conclude, then, that the outflow is AGN-driven.

4.2 Outflow Driving Mechanisms

A first look from Figure 6 indicates that steep velocity and density gradients ($\beta \leq 1$ and $\alpha \geq 2$, respectively) produce weaker outflows than shallow gradients. To understand the nature of strong vs weak outflows, both in the context of Mrk 462 and more generally, we want to know what underlying mechanism(s) and physical conditions produce or otherwise facilitate the observed profiles. The Heckman et al. (2015) criterion suggests that mass-conserving or even mass-sweeping winds ($\alpha \leq 2$) produce the strongest outflows, especially if the velocity gradient is shallow (i.e., acceleration continues out to larger galactic radii).

Now, we consider the possible mechanism(s) behind the outflow. Murray et al. (2005) define velocity profiles for several momentum-driven outflow mechanisms: optically thin and thick radiation pressure and ram pressure. Ram pressure and optically thin radiation pressure are formally similar, with acceleration $\propto r^{-2}$ and a velocity profile of

$$\left(\frac{v}{2v_0}\right)^2 = \frac{L}{L_E} \left[1 - \frac{1}{x}\right] - \ln(x) \quad (21)$$

where $L_E \propto v_0^2$ is the Eddington luminosity at the launch radius and L is the luminosity of the driving mechanism⁵. If, instead, the

⁵ In the case of ram pressure, L/L_E is equivalent to the V_c^2/σ^2 term in Equation A2 of Murray et al. (2005).

Table 3. Parameters for different outflow driving mechanisms determined by least squares fitting of model profiles to the observed velocity profile.

model	L/L_E	L/L_M
thin / ram	12.88	–
thick	–	5.07
dusty / clumpy	3.75	2.95

radiation pressure is optically thick, then the velocity profile becomes

$$\left(\frac{v}{2v_0}\right)^2 = \left[\frac{L}{L_M} - 1\right] \ln(x) \quad (22)$$

where $L_M \propto \sigma_v^4$ is the lower limit on luminosity for a momentum driven wind. We consider a third scenario which combines the optically thick and optically thin scenarios in the equation of motion. Since the thin and thick radiation pressure terms are separate, the resulting velocity profile is

$$\left(\frac{v}{2v_0}\right)^2 = \frac{L}{L_E} \left[1 - \frac{1}{x}\right] + \left[\frac{L}{L_M} - 1\right] \ln(x). \quad (23)$$

This third scenario corresponds to dusty radiation pressure driving, which is optically thick in the UV and optically thin in the infrared (cf. formalism in Ishibashi & Fabian 2015; Ishibashi et al. 2018, 2021). One might alternatively interpret the above expression as an optically thin outflow populated by optically thick clouds (i.e., a “clumpy” outflow)⁶. Given the complexities of the ISM, the third scenario is likely a combination of both clumpiness and dusty radiation pressure. A substantial fraction of dust (in excess of 10% of the pre-existing dust) is known to survive in shocked environments such as wind-blown bubbles (e.g., Everett & Churchwell 2010), AGN jets (e.g., Villar-Martín et al. 2001), and SNe remnants (e.g., Slavin et al. 2020), indicating that even under extreme conditions, a dusty radiatively-driven outflow is a plausible scenario to consider. We determine L/L_E and L/L_M for the best-fit β velocity profile using linear least squares and list the results in Table 3. We show best-fit model profiles normalized to v_∞ in Figure 8.

From the fit results shown in Figure 8, the radiatively-driven optically thick and clumpy outflow models provide much better descriptions of the observed profile than that of the optically thin / ram pressure. As such, we conclude that the outflow in Mrk 462, for which $\beta = 1.369$, is radiatively driven.

In context of Figure 6, the association of higher β with optically thick or dusty radiation pressure suggests that radiatively driven outflows are relatively strong at fixed α . Given that dust is the primary source of the optical depth and that dust opacities are orders of magnitude higher in the UV than at longer wavelengths (e.g., Draine 2003), the optically thick outflow almost certainly must be driven by UV photons. Thus, the role of UV luminosity as a feedback mechanism in Mrk 462, and galaxies hosting star formation and/or AGN in general, is pivotal. Effects due to these outflows will be particularly pronounced in dwarf galaxies where the gravitational potential is weak (and therefore v_0 is lower), resulting in much stronger feedback (recall $\dot{p}/\dot{p}_0 \propto v_0^{-2}$ and $L/L_M \propto \sigma_v^{-4}$).

Which of the thick shell or dusty/clumpy geometries best describes the radiative outflow? Qualitatively, we favor the dusty/clumpy scenario simply because the uniform shell is highly idealized and oversimplifies the complexities of the ISM. However, the fits to the velocity profile for both uniformly optically thick and dusty radiation

⁶ As discussed in Murray et al. (2005), the “optically thin” model for ram pressure is by definition a clumpy outflow with clouds entrained in a hot wind.

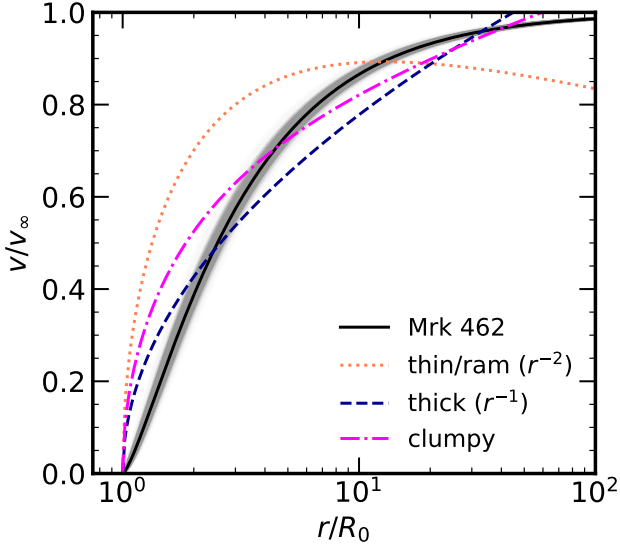


Figure 8. Velocity profile inferred from the [O III] line in Mrk 462 (solid black) compared to optically thick radiation pressure (dashed dark blue) and optically thin radiation or ram pressure (dotted orange) velocity profiles from Murray et al. (2005), along with the profile expected in a dusty/clumpy radiation pressure scenario (dash-dotted magenta). Grey shaded region indicates the 3σ confidences on the shape of the profile.

pressure scenarios shown in Figure 8 seem comparably accurate. An initial quantitative assessment of the reduced sum squared residuals, χ^2_V , shows that the dusty model outperforms the thick model by a factor of 2. To determine whether we can reject the simpler optically thick model on this basis, we calculate the log likelihood ratio $\lambda_r = \Delta\chi^2_r$. For sufficiently large data sets, λ_r is drawn from a χ^2 distribution with degrees of freedom equal to the difference in the number of parameters. Since we can make x arbitrarily large, the survival function for the χ^2 distribution approximates the probability that the two sets of residuals are similar, i.e., the probability that the uniform optically thick shell (the null hypothesis) is a sufficient description of the velocity profile when compared to the dusty shell (the alternate hypothesis). Reduced residuals from our fits give $\lambda_r = 0.788$, which corresponds to a p -value of 0.376. While our statistical assessment cannot rule out the null hypothesis that the optically thick mechanism alone drives the outflow, the dusty scenario more closely describes the velocity profile in Mrk 462. Thus, we favor a picture in which the outflow is dusty and radiatively driven.

The best fit parameters for the dusty outflow also provide insight into the relative luminosity of the driving mechanism (see Table 3). For the optically thick component, we find $L/L_M \approx 3$. When $L > L_M$, a galaxy experiences winds capable of removing gas, which can regulate star formation and/or black hole growth (Murray et al. 2005). As a result, gas-fueled activity will likely be episodic. With $L/L_E \approx 4$, the optically thin component of the outflow facilitates acceleration within a few R_0 of x_{out} and contributes to the velocity profile for nearly an order of magnitude in radius (see prediction that $L/L_E \sim 3$ drives an outflow to at least $10R_0$ in Murray et al. 2005) before optically thick radiation pressure becomes the sole source of momentum deposition.

While the velocity field can inform the mechanisms involved in driving the outflow, the best-fit driving luminosity L can indicate more about the source of the outflow. To begin, the Eddington lumi-

nosity L_E is given by

$$L_E = \frac{4\pi GM_\star c}{\kappa}. \quad (24)$$

Because the AGN SED is typically most luminous in the FUV, we assume $\kappa \approx 10^5 \text{ cm}^2 \text{ g}^{-1}$, which is characteristic of dust opacity at 1000 \AA (e.g., Draine 2003). We obtain an implied driving luminosity of $L = 3.75L_E \approx 10^{43} \text{ erg s}^{-1}$. Murray et al. (2005) give the critical luminosity L_M as

$$L_M = \frac{4f_g c \sigma_0^4}{G} \quad (25)$$

where $f_g \sim 0.001$ is the gas mass fraction estimated from the $H\beta$ flux following Harrison et al. (2014) and the stellar mass from Moran et al. (2014). Assuming σ_0 is well-represented by the velocity dispersion determined from the narrow component of the [O III] line, we obtain a driving luminosity $L = 2.95L_M \approx 1 \times 10^{43} \text{ erg s}^{-1}$. Following the $L = 4.3 \times 10^{41} \text{ SFR erg s}^{-1}$ scaling relation in Xu et al. (2022), the SFR in Mrk 462 obtained in §4.1 implies a luminosity of $10^{41} \text{ erg s}^{-1}$, which cannot account for either of the driving luminosities. However, the driving luminosity is sufficiently below the estimated L_{AGN} by about 0.5 dex, suggesting that AGN can account for the luminosities associated with the velocity profile.

Our examination of both the relative properties and velocity profile of the outflow in Mrk 462 indicate several key aspects of the underlying mechanisms. First, the outflow is driven by radiation pressure imparting momentum to clouds. Second, dust likely provides the opacity for the radiation pressure, having both optically thin and optically thick components. The dusty clouds which constitute the outflow are more likely distributed in clumps than in a uniform shell. Third, the luminosity necessary to drive the dusty outflow is 3–4 times the critical values, which can regulate gas-fueled activity in a galaxy. Finally, the properties and velocity profile require source luminosities which stellar populations alone cannot produce, suggesting that the central AGN must provide the momentum needed to drive the outflow. Together, these characteristics indicate that Mrk 462 is producing a self-regulating, albeit relatively weak, radiatively-driven dusty outflow powered by the AGN.

5 CONCLUSION AND FUTURE WORK

Motivated by the asymmetric, broad forbidden nebular lines in Mrk 462, we have presented a physically motivated line profile based on the traditional outflow interpretation of similar profiles observed in other galaxies. We have demonstrated how underlying velocity and density profiles combine to yield the observed line profile, establishing a formalism which is flexible and readily applicable to other nebular lines. After application of this line profile to the [O III] $\lambda\lambda 4959, 5007$ doublet in Mrk 462, we illustrate how properties of the outflow can be derived, including characteristic momentum and energy injection rates. We also draw on previous model velocity profiles to interpret the best-fit velocity profile. From this comparison, we conclude that the outflow in Mrk 462 is relatively weak (although still quite strong), radiatively driven, and dusty/clumpy.

While we have provided a foundation for the analysis of outflows traced by asymmetric nebular emission lines, our results are merely that: foundational. Adjustments to our model to include additional effects such as dust may provide improvements to the line profile and results. Future work will also include application of our methods to the study of outflows in various contexts, specifically their role in galaxy evolution and the escape of ionizing photons.

Dust is likely entrained in the outflow, as evidenced by the radiative driving generated by the UV photon flux. The presence of dust could exacerbate the asymmetry in the outflow profile by preferentially extinguishing the emission from material moving away from the observer along the line of sight, thereby diminishing the red wing of the line profile relative to the blue (cf. Heckman et al. 1981; Veilleux 1991). Such effects should be explored in detail in future work to determine if they are significant and, if so, how the inclusion of dust extinction within the outflow might affect the emergent line profile and derived outflow properties.

A velocity offset may exist between the Gaussian core and outflow profiles, too. Such an offset might arise from a rest velocity of the outflow launch which is not spatially coincident with the narrow Gaussian component. That is, the outflow may have a different rest velocity at the launch radius than the dynamically quiescent photoionized clouds in star-forming regions or the AGN NLR. Such a velocity offset might explain the red-winged outflow profiles observed in some galaxies (e.g. Ruschel-Dutra et al. 2021).

One of the key applications of our methods will be the role of feedback in the escape of Lyman continuum photons. Previous studies of Lyman continuum emitters (LCEs) and Green Peas (e.g. Chisholm et al. 2017b; Jaskot et al. 2017, respectively) found *reduced* outflow velocities, indicative of suppressed superwinds. Indeed, the well-studied LCE Haro 11 has $v_{out} \approx 160 \text{ km s}^{-1}$ (Heckman et al. 2015), less than half that of Mrk 462. However, the extreme [O III] wings in Mrk 71, a Green Pea and a LCE candidate, exhibit v_{∞} in excess of $3,000 \text{ km s}^{-1}$ (Komarova et al. 2021). The well-studied $z = 2.37$ Sunburst Arc, a known LCE (Rivera-Thorsen et al. 2019), exhibits characteristic and terminal outflow velocities ($v_{out} = 327 \text{ km s}^{-1}$ and $v_{\infty} = 750 \text{ km s}^{-1}$, respectively) in its LyC-leaking regions nearly identical to those we found for Mrk 462 (Mainali et al. 2022). Similar high velocities have been found in [O III] profiles of local ($z \sim 0.3$) known LCEs (Rodriguez et al. in prep, Komarova et al. in prep). The confounding results, as well as the ultimate cosmological implications for *how* galaxies reionized the universe, should be addressed through use of our novel analysis methods. Doing so will determine whether Lyman continuum escape is facilitated by feedback and outflows, to what degree, and which physical mechanisms are involved.

Another important question to address will be the roles of AGN and star-formation feedback in galaxy evolution. Characterizing the spatial distribution of UV and IR fluxes in Mrk 462 and other galaxies with outflows will be key to understanding the nature of dusty radiative feedback. Analysis of outflow line properties in both AGN and starbursts will be key, particularly when both are present, to assess whether and how radiative outflows affect star formation and black hole growth. Investigating the evolution of these outflow properties over cosmic time will also be critical for assessing when outflows are at their strongest and what role they play in determining the stellar mass of their host galaxies.

SOFTWARE

ASTROPY (Astropy Collaboration et al. 2013, 2018), CORNER (Foreman-Mackey 2016), EMCEE (Foreman-Mackey et al. 2013), MATPLOTLIB (Hunter 2007), NUMPY (van der Walt et al. 2011), PYNEB (Luridiana et al. 2015), SCIPY (P. Virtanen 2020), SYMPY (Meurer et al. 2017)

ACKNOWLEDGEMENTS

We thank the anonymous referee for feedback which improved the clarity of this paper.

DATA AVAILABILITY

The calibrated data underlying this article were provided by Eleazer et al (in prep) by permission. The raw data are publicly available through the Gemini data archive at <https://archive.gemini.edu/searchform>.

REFERENCES

- Abbott D. C., 1977, PhD thesis, University of Colorado, Boulder
- Amorín R., Vílchez J. M., Hägele G. F., Firpo V., Pérez-Montero E., Papaderos P., 2012, *ApJ*, **754**, L22
- Armus L., et al., 2022, arXiv e-prints, p. arXiv:2209.13125
- Astropy Collaboration et al., 2013, *A&A*, **558**, A33
- Astropy Collaboration et al., 2018, *aj*, **156**, 123
- Barlow M. J., Cohen M., 1977, *ApJ*, **213**, 737
- Binette L., Drissen L., Ubeda L., Raga A. C., Robert C., Krongold Y., 2009, *A&A*, **500**, 817
- Calzetti D., 2013, in Falcón-Barroso J., Knapen J. H., eds., *Secular Evolution of Galaxies*. p. 419, doi:10.48550/arXiv.1208.2997
- Carr C., Scarlata C., Panagia N., Henry A., 2018, *ApJ*, **860**, 143
- Castor J. I., Lamers H. J. G. L. M., 1979, *ApJS*, **39**, 481
- Castor J. I., Abbott D. C., Klein R. I., 1975, *ApJ*, **195**, 157
- Chisholm J., Tremonti C. A., Leitherer C., Chen Y., Wofford A., Lundgren B., 2015, *ApJ*, **811**, 149
- Chisholm J., Tremonti Christy A., Leitherer C., Chen Y., 2016, *MNRAS*, **463**, 541
- Chisholm J., Tremonti C. A., Leitherer C., Chen Y., 2017a, *MNRAS*, **469**, 4831
- Chisholm J., Orlitová I., Schaerer D., Verhamme A., Worseck G., Izotov Y. I., Thuan T. X., Guseva N. G., 2017b, *A&A*, **605**, A67
- Chisholm J., Bordoloi R., Rigby J. R., Bayliss M., 2018a, *MNRAS*, **474**, 1688
- Chisholm J., Tremonti C., Leitherer C., 2018b, *MNRAS*, **481**, 1690
- Draine B. T., 2003, *ARA&A*, **41**, 241
- Eggen N. R., Scarlata C., Skillman E., Jaskot A., 2022, arXiv e-prints, p. arXiv:2207.02245
- Everett J. E., Churchwell E., 2010, *ApJ*, **713**, 592
- Foreman-Mackey D., 2016, *The Journal of Open Source Software*, **1**, 24
- Foreman-Mackey D., Hogg D. W., Lang D., Goodman J., 2013, *PASP*, **125**, 306
- Gallagher R., Maiolino R., Belfiore F., Drory N., Riffel R., Riffel R. A., 2019, *MNRAS*, **485**, 3409
- Gazagnes S., Chisholm J., Schaerer D., Verhamme A., Rigby J. R., Bayliss M., 2018, *A&A*, **616**, A29
- Harrison C. M., Alexander D. M., Mullaney J. R., Swinbank A. M., 2014, *MNRAS*, **441**, 3306
- Heckman T. M., Miley G. K., van Breugel W. J. M., Butcher H. R., 1981, *ApJ*, **247**, 403
- Heckman T. M., Armus L., Miley G. K., 1990, *ApJS*, **74**, 833
- Heckman T. M., Kauffmann G., Brinchmann J., Charlot S., Tremonti C., White S. D. M., 2004, *ApJ*, **613**, 109
- Heckman T. M., et al., 2011, *ApJ*, **730**, 5
- Heckman T. M., Alexandroff R. M., Borthakur S., Overzier R., Leitherer C., 2015, *ApJ*, **809**, 147
- Henry A., Scarlata C., Martin C. L., Erb D., 2015, *The Astrophysical Journal*, **809**, 19
- Hunter J. D., 2007, *Computing in Science Engineering*, **9**, 90
- Ishibashi W., Fabian A. C., 2015, *MNRAS*, **451**, 93
- Ishibashi W., Fabian A. C., Maiolino R., 2018, *MNRAS*, **476**, 512
- Ishibashi W., Fabian A. C., Arakawa N., 2021, *MNRAS*, **502**, 3638

- Jaskot A. E., Oey M. S., Scarlata C., Dowd T., 2017, *ApJ*, **851**, L9
- Klein R. I., McKee C. F., Colella P., 1994, *ApJ*, **420**, 213
- Komarova L., Oey M. S., Krumholz M. R., Silich S., Kumari N., James B. L., 2021, *ApJ*, **920**, L46
- Krumholz M. R., Thompson T. A., Ostriker E. C., Martin C. L., 2017, *MNRAS*, **471**, 4061
- Lamers H. J. G. L. M., Morton D. C., 1976, *ApJS*, **32**, 715
- Lamers H. J. G. L. M., Cerruti-Sola M., Perinotto M., 1987, *ApJ*, **314**, 726
- Leroy A. K., et al., 2015, *ApJ*, **814**, 83
- Leung G. C. K., et al., 2019, *ApJ*, **886**, 11
- Liu G., Zakamska N. L., Greene J. E., Nesvadba N. P. H., Liu X., 2013, *MNRAS*, **436**, 2576
- Ludwig R. R., Greene J. E., Barth A. J., Ho L. C., 2012, *ApJ*, **756**, 51
- Luridiana V., Morisset C., Shaw R. A., 2015, *A&A*, **573**, A42
- Mainali R., et al., 2022, arXiv e-prints, p. [arXiv:2210.11575](https://arxiv.org/abs/2210.11575)
- Martin C. L., 2005, *ApJ*, **621**, 227
- Martin C., et al., 2003, in Blades J. C., Siegmund O. H. W., eds, Society of Photo-Optical Instrumentation Engineers (SPIE) Conference Series Vol. 4854, Future EUV/UV and Visible Space Astrophysics Missions and Instrumentation.. pp 336–350, doi:10.1117/12.460034
- Meurer A., et al., 2017, *PeerJ Computer Science*, **3**, e103
- Mihalas D., Kunasz P. B., Hummer D. G., 1975, *ApJ*, **202**, 465
- Moran E. C., Shahinyan K., Sugarman H. R., Vélez D. O., Eracleous M., 2014, *AJ*, **148**, 136
- Murray N., Quataert E., Thompson T. A., 2005, *ApJ*, **618**, 569
- Nakamura F., McKee C. F., Klein R. I., Fisher R. T., 2006, *ApJS*, **164**, 477
- Noerdlinger P. D., Rybicki G. B., 1974, *ApJ*, **193**, 651
- Osterbrock D. E., 1991, *Reports on Progress in Physics*, **54**, 579
- Osterbrock D., Ferland G., 2006, *Astrophysics of Gaseous Nebulae and Active Galactic Nuclei*. University Science Books
- P. Virtanen R. Gommers T. O., 2020, *Nature Methods*, **17**, 261–272
- Pauldrach A., Puls J., Kudritzki R. P., 1986, *A&A*, **164**, 86
- Peimbert M., Peimbert A., Delgado-Inglada G., 2017, *Publications of the Astronomical Society of the Pacific*, **129**, 082001
- Pelat D., Alloin D., 1980, *A&A*, **81**, 172
- Pelat D., Alloin D., Fosbury R. A. E., 1981, *MNRAS*, **195**, 787
- Prochaska J. X., Kasen D., Rubin K., 2011, *ApJ*, **734**, 24
- Reddy N. A., Steidel C. C., Pettini M., Bogosavljević M., 2016, *ApJ*, **828**, 107
- Reyes R., Mandelbaum R., Gunn J. E., Pizagno J., Lackner C. N., 2011, *MNRAS*, **417**, 2347
- Riffel R. A., 2010, *Ap&SS*, **327**, 239
- Rivera-Thorsen T. E., et al., 2019, *Science*, **366**, 738
- Rupke D. S., Veilleux S., 2005, *ApJ*, **631**, L37
- Rupke D. S. N., Veilleux S., 2011, *ApJ*, **729**, L27
- Rupke D. S. N., Veilleux S., 2013, *ApJ*, **768**, 75
- Rupke D. S., Veilleux S., Sanders D. B., 2002, *ApJ*, **570**, 588
- Rupke D. S., Veilleux S., Sanders D. B., 2005a, *ApJS*, **160**, 87
- Rupke D. S., Veilleux S., Sanders D. B., 2005b, *ApJS*, **160**, 115
- Ruschel-Dutra D., et al., 2021, *MNRAS*, **507**, 74
- Salviander S., Shields G. A., Gebhardt K., Bonning E. W., 2007, *The Astrophysical Journal*, **662**, 131
- Scarlata C., Panagia N., 2015, *ApJ*, **801**, 43
- Schönell A. J., Storch-Bergmann T., Riffel R. A., Riffel R., Bianchin M., Dahmer-Hahn L. G., Diniz M. R., Dametto N. Z., 2019, *MNRAS*, **485**, 2054
- Slavin J. D., Dwek E., Mac Low M.-M., Hill A. S., 2020, *ApJ*, **902**, 135
- Sobolev V. V., 1944, *Soviet Ast.*, **21**, 1944
- Sobolev V. V., 1957, *Soviet Ast.*, **1**, 678
- Sobolev V. V., 1960, Moving envelopes of stars
- Steidel C. C., Erb D. K., Shapley A. E., Pettini M., Reddy N., Bogosavljević M., Rudie G. C., Rakic O., 2010, *ApJ*, **717**, 289
- Veilleux S., 1991, *ApJS*, **75**, 383
- Veilleux S., Maiolino R., Bolatto A. D., Aalto S., 2020, *A&ARv*, **28**, 2
- Villar-Martín M., De Young D., Alonso-Herrero A., Allen M., Binette L., 2001, *MNRAS*, **328**, 848
- Villar-Martín M., Humphrey A., Delgado R. G., Colina L., Arribas S., 2011, *MNRAS*, **418**, 2032
- Vink J. S., Sander A. A. C., 2021, *MNRAS*, **504**, 2051
- Vink J. S., de Koter A., Lamers H. J. G. L. M., 2001, *A&A*, **369**, 574
- Whittle M., 1985, *MNRAS*, **213**, 1
- Xu X., et al., 2022, *ApJ*, **933**, 222
- van der Marel R. P., Franx M., 1993, *ApJ*, **407**, 525
- van der Walt S., Colbert S. C., Varoquaux G., 2011, *Computing in Science Engineering*, **13**, 22

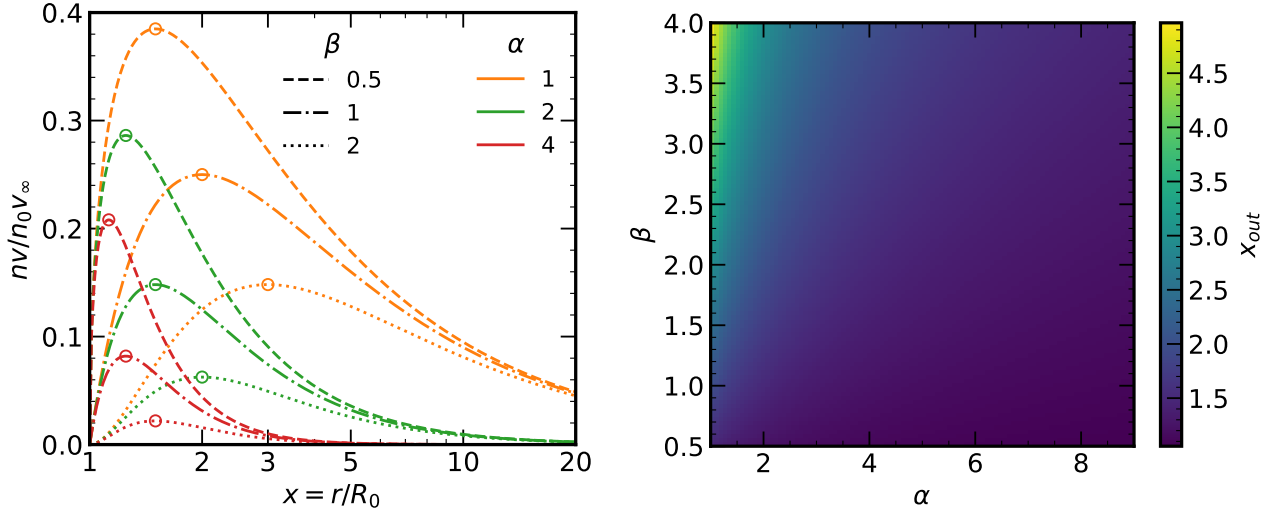


Figure B1. *Left:* Momentum density profiles for different values of α and β . The location of maximum momentum density for each profile is indicated by an open circle. *Right:* The outflow radius x_{out} at maximum momentum density mapped over α and β .

APPENDIX A: EXAMPLE PROFILE IMPLEMENTATION IN PYTHON

```

1 from numpy import zeros, array, sqrt, trapz
2 from scipy.optimize import brentq
3 from scipy.integrate import romberg
4 # function to calculate wind profile, assuming vinf in c units
5 def wind_profile(wave, wave0, vinf, alpha, beta):
6     # observed velocity from wavelengths, in vinf/c units
7     u = abs(wave-wave0)/wave0 /vinf
8     # normalized radius from velocity
9     x = lambda w: ( 1-w**(1/beta) )**-1
10    # normalized density profile n/n0
11    n = lambda w: ( 1-w**(1/beta) )**alpha
12    # with no occultation, the minimum velocity is just the observed velocity
13    wmin = u[u<1]
14    # when occultation by source occurs, solve for minimum contributing velocity
15    wmin[wave[u<1]>wave0] = array(list( map( lambda ui: \
16        brentq(lambda wl: ui - wl/x(wl)*sqrt(x(wl)**2-1), ui, 1), \
17        u[(u<1)&(wave>wave0)]) ) )
18    # profile integrated at each velocity range
19    phi = zeros(len(u))
20    phi[u<1] = array(list( map( lambda wl: \
21        romberg(lambda w: n(w)**2, wl, 1), \
22        wmin) ) )
23    # normalize so integral goes to 1 and units are wavelength^-1
24    norm = trapz(phi, x=wave)
25    return phi/norm

```

APPENDIX B: RADIUS OF MAXIMUM MOMENTUM DENSITY

We show the momentum density as a function of radius in the left panel of Figure B1. Regardless of α and β , a maximum in nv consistently occurs; however, the location of this maximum clearly varies with α and β . To obtain the radius x_{out} at which the outflow momentum density is maximal, we calculate x_{out} for the range of typical values of α and β (see §2.1) by root-finding. We visualize the effects of α and β on the peak of the momentum distribution in the right panel of Figure B1. Values of x_{out} increase with decreasing α and increasing β .

From a well-sampled grid of typical values of α and β , we find that $x_{out} \in (1, 5]$ and that x_{out} increases with β and decreases with α . We map values of x_{out} over α and β in the right panel of Figure B1. Typical values of x_{out} are close (but not equal) to unity with an upper 95th percentile on x_{out} of 2.80.

This paper has been typeset from a $\text{\TeX}/\text{\LaTeX}$ file prepared by the author.